VALORIZATION OF TANGERINE PEELS THROUGH THE SYNTHESIS OF MAGNETIC NANOCATALYSTS

J. R. P. Oliveira[1], J. L. Diaz de Tuesta[2,3], H. T. Gomes[2], J.S. Napoli[1], L.S. Ribas[1], G. G. Lenzi[1]

[1]Departamento de Engenharia Química, Universidade Tecnológica Federal do Paraná, Rua Doutor Washington Subtil Chueire, 330, Ponta Grossa, PR 84017-220, Brazil;
[2]Centro de Investigação de Montanha (CIMO), Instituto Politécnico de Bragança, Campus de Santa Apolónia, 5300-253, Bragança, Portugal;
[3]Department of Chemical and Environmental Technology, Rey Juan Carlos University, C. Tulipán, s/n, 28933 Móstoles, Spain.

ABSTRACT This study describes the synthesis of an innovative nanomaterial composed of cobalt ferrite functionalized in niobium pentoxide $CoFe_2O_4@Nb_2O_5$ synthesized by green synthesis using tangerine peel extract. The material values the combination of a magnetic material (which allows easy recovery after application) with niobium pentoxide (whose metal is abundant in Brazilian territory). The synthesis was carried out with some temperature variations of the niobium calcination before joining with iron and cobalt salts and tangerine extract, the resulting materials were applied as catalysts in the degradation of Paracetamol by photocatalysis. The new materials were characterized by the following techniques: surface and pore analysis (S_{BET}, S_{EXT}, S_{mic}, V_{mic} and V_{TOTAL}), photoacoustic spectroscopy (PAS), point of zero charge (pH_{PZC}), scanning electron microscopy (SEM/EDS) and X-ray diffraction (XRD). The studied reaction parameters included pH, catalyst concentration and radiation variation (different powers for the mercury vapor lamp). The results indicated that the $CoFe_2O_4@Nb_2O_5$ nanocatalysts were efficient in the degradation of Paracetamol (up to 99% degradation), showing better results under conditions of pH 2.59, catalyst concentration 158.58 mg L^{-1}, under irradiation of the 250 W mercury vapor lamp (greater than 28 mW /cm²) at 240 minutes of the reaction.

KEYWORDS: Green synthesis, Heterogeneous photocatalysis, Emerging pollutants.

1. Introduction

Optimization in catalysis can minimize the use of energy and raw materials, reducing waste to the environment [1] Catalysis can also be applied to the degradation of harmful components into more environmentally friendly components. The advent of nanosciences has promoted the molecular approach, which is currently very useful for the production of selective and efficient heterogeneous catalysts that can be removed after the reaction and reused. Nanocrystals of just a few nanometers have high catalytic efficiency, related to their high contact area [2].

Nanocatalysts are nanomaterials (NMs) with a catalyst function that have dimensions in the order of nanometer (10^{-9} m). Magnetic nanocatalysts (MNC) are studied due to advantages such as easy recovery at the end of the process and the efficiency of the catalytic activity of the metals that compose them [3]. Due to their potential applications, several methods of synthesis of magnetic nanoparticles (MNPs) have been studied in recent years.

In this work two synthesis methods were conciliated to produce nanocatalysts, solution combustion synthesis (SCS) and reduction using plant extracts (RPE). The method used can be characterized as Green Synthesis, because it fits the 12 principles of green chemistry, specifically the principles 1, 3, 5 and 7, which concern: 1.Prevent waste; 3.Design less hazardous chemical syntheses; 5.Use safer solvents and reaction conditions; 7.Use renewable feedstocks [4-6].

Gingasu *et. al.* (2016) produced cobalt ferrite ($CoFe_2O_4$) using hibiscus flower extract (*Hibiscus rosa-sinensis*) [7] and sesame seed extract (*Sesamum indicum L*) [8]. In both works, the synthesis occurred using modified solution combustion synthesis, adding the extracts mentioned on cobalt and iron nitrates.

The possibility of synthesizing nanocatalysts using *C. reticulata* extract is promising to know that it comes from a citrus fruit containing citric acid, and that this in turn can be used in SCS. There are already some reported works on the synthesis of NMs from tangerine peels [9-12].

Cobalt ferrite ($CoFe_2O_4$) is among the most relevant ferrites due to the peculiarities of its properties such as great physical and chemical stability [7,13,14]. This material can be applied to magneto-sensitive systems[13,15], to remove pollutants from water [3,16,17], in drug delivery [18,19] and in acid mine drainage treatments [20]. Niobium is an abundant transition metal in Brazil, which has about 98% of the world's known niobium reserves [21]. Niobium and its properties have been studied as photocatalysts in the oxide form (Nb_2O_5) and/or combined with other compounds. Some studies report the efficiency of the photocatalytic activity of niobium oxide in the degradation of dyes in textile industries [22], in the degradation of the herbicide Methylviologen [23] and in the abatement of air pollution [24]. Concerning to formation of complex compounds, combinations with niobium already reported in the literature [25-32].

In this perspective, the feasibility of synthesizing efficient nanophotocatalysts using magnetic materials, such as cobalt ferrites, together with niobium oxide (abundant in the Brazilian territory), looks promising for application in the degradation of pollutant found in water.

Photocatalysis is among the various types of catalytic reactions that are characterized as advanced oxidation processes (AOPs). In AOPs, highly oxidizing hydroxyl radicals ($^{\bullet}OH$) are produced (standard reduction potential between +2.8 V and +2.0 V at pH 0 and 14, respectively), capable of degrading organic pollutants generating CO_2, H_2O and inorganic ions [3,33-35].

Photocatalysis is a reaction carried out in the presence of light and of a semiconductor catalyst (photocatalyst) [2]. These reactions using semiconductors has been shown to be highly effective in the degradation of pollutants that are difficult to remove by other methodologies. The semiconductors mostly used as catalysts in this process are binary semiconductors like TiO_2, ZnO, Fe_2O_3, CdS and ZnS due to a favorable combination of their electronic structure, light absorbing properties, load transport characteristics and excited-state lifetime [2,36]. Photocatalys is an efficient process under ambient temperature and pressure conditions and by having low cost in relation to other oxidation processes [37]. And is used to degrade various harmful compounds in water treatment [38,39], mainly organic compounds[16,36].

The concepts of emerging pollutants (EPs) and contaminants of emerging concern (CECs) intersect with respect to pollutants that are being identified in low concentration in wastewater, which may require specific treatment for their removal, with only conventional treatments being inefficient. Advanced oxidative processes (AOPs) are among those alternatives. Drugs deserve special attention, as this type of substances are widely consumed by humans and administered to animals, resulting in discharges, usually of unknown concentrations, to the environment, especially in developing countries [40,41].

Paracetamol (or acetaminophen) is widely used worldwide as a drug without prescription. The main concern about increasing the consumption of this drug is that after ingested about 90% of a therapeutic dose is excreted in the urine after 24 hours. The composition of this excretion contains around 1-4% of unchanged paracetamol and 60-90% of metabolites (i.e., any intermediate compound in the metabolism's enzymatic reactions). It is found in sewage in the order of nano or micrograms per liter, being classified as an emerging pollutant. However, the increase in consumption raises the concern of accumulation of this drug in the food chain, since it is not easily degraded by the usual treatment methods at Wastewater Treatment Plants (WWTPs)[40,42].

However, the objective of this work was use extracts of tangerine peel (*Citrus reticulata)* to synthesize magnetic catalysts with cobalt (Co), iron (Fe) and niobium (Nb) for catalytic application to paracetamol (PCT) degradation using photocatalysis.

2. Experimental Procedure

2.1 Chemicals

Acetonitrile (CH_3CN), supplied by Merk, Germany; Anhydrous citric acid (C6H8O7), supplied by Perquim Rep. Com., Analytical Science, Ponta Grossa- PR; Anhydrous sodium sulfate (Na2SO4), supplied by Neon, Suzano-SP; Cobalt nitrate (Co(NO3)2.6H2O), supplied by Synth, Diadema-SP; Formic acid (CH2O2), supplied by Synth, Diadema-SP ; Iron nitrate (Fe(NO3)3.9H2O), supplied by Synth, Diadema-SP; Niobium pentoxide (Nb2O5), supplied by CBMM – Companhia Brasileira de Metalurgia e Mineração, Araxá-MG; Sodium hydroxide (NaOH), supplied by Dinâmica Química Contemporânea Ltda., Indaiatuba – SP; Sulfuric acid (H2SO4), supplied by Dinâmica Química Contemporânea Ltda., Indaiatuba – SP.

2.2 Catalysts preparation

Tangerine peels extract

The first step to obtaining the catalyst is drying the tangerine peels, Figure 1 – Step 1 (A). These peels further subjected to washing under continuous flow of water and previously drying under sun to avoid fungal contamination. After, the tangerine peels are placed in drying oven (SL 102, SOLAB) at 80 ± 5 °C for 18 h. Sequentially, the tangerine peels were crushed in an analytical mill (Q298A21, QUIMIS) and sieved to obtain a diameter between 250 µm (60 mesh) and 106 µm (150 mesh) (wire cloth test sieve, Bertel), Step 1 (B). Finally, the tangerine peels were stored until the next step.

To obtain the tangerine peels extract the following methodology was optimized, Step 1 (C), using an analytical balance (AUY220, SHIMADZU), 4.0 g of crushed tangerine peels were placed in a 250 mL round-bottom flask with 100 mL of distilled water, which was placed under magnetic stirring at room temperature (25 °C) for 3 h (C-MAG HS 7, IKA). After, the temperature was increased to 60 °C for 1 h [7,43], the dispersion further centrifuged at 4000 rpm (revolutions per minute) for 5 minutes, to separate the tangerine peels from the supernatant (80- 2B centrifuge, CENTRIBIO). After centrifugation, the supernatant was filtered through a paper filter, to remove any possible peel that was still present in the solution. Finally, the obtained extract solution was stored in a freezer until use, completing the first step, Step 1 (D). The reducing power (EC_{50} RP) of this extract was 1.68 ± 0.03 mg mL^{-1} (Analyzed by Centro de Investigação de Montanha - CIMO, Instituto Politécnico de Bragança, Bragança, Portugal). The EC_{50} values correspond to the concentration of extract that provides 50% of reducing power or antioxidant activity. Lower EC_{50} values means higher antioxidant capacity of the samples [44]. The catalysts synthesis of the, the second step is niobium pentoxide calcination, Step 2 (E). Approximately 10 g of niobium pentoxide (Nb_2O_5) was weighted in a porcelain crucible. Then, each sample was calcined in a calcination furnace, this process resulted in seven samples of niobium oxide: Nb, Nb100, Nb200, Nb300, Nb400, Nb500 and Nb600.

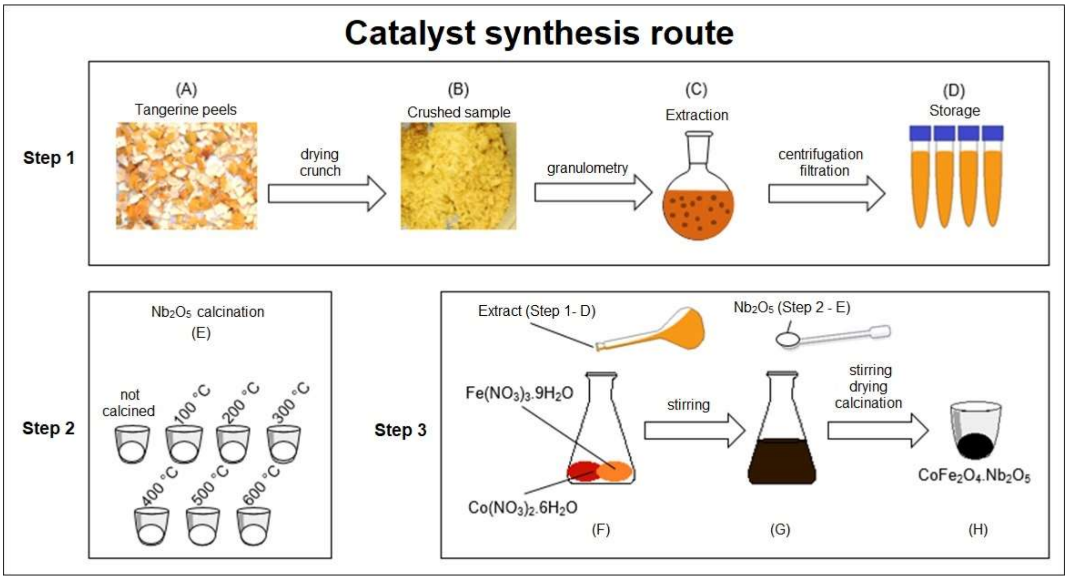

Figure 1. Route to the green synthesis method of functionalized cobalt ferrite in niobium pentoxide.

On the third step, the cobalt ferrite functionalized catalysts in niobium pentoxide ($CoFe_2O_4.Nb_2O_5$) have been synthesized. The salts Fe^{3+} (11.4 mmol) and Co^{2+} (5.7 mmol) were weighted in a 150 mL Erlenmeyer (i.e. approximately 4.61 ± 0.01 g of $Fe(NO_3)_3.9H_2O$ and 1.66 ± 0.01 g of $Co(NO_3)_2.6H_2O$). After were added 25 mL of tangerine peels extract (obtained in first step), the resultant solution showing immediately black color, Figure 1 - Step 3 (G). The Erlenmeyer was stirred in the shaker (TE-424, TECNAL) at 200 ± 2 rpm, 25 ± 2°C for 15 minutes. The theoretical weight of the cobalt ferrite to be formed was 1.33 g, so this amount of niobium pentoxide was weighted and added in the Erlenmeyer after the above referred 15 minutes, Step 3 (G). The mixture was stirred more 15 minutes under the same conditions. In sequence, the mixture was transferred to a porcelain crucible, which stayed in a drying oven for 4.5 hours at 100 ± 10 °C, until forming a gel. Finally, the porcelain crucible with the gel was placed in a calcination furnace (N1200, NOVUS) with a heating ramp. After calcination, the resulting material in the porcelain crucible is cobalt ferrite functionalized in niobium, Figure 1 – Step 3 (H).

According with the calcined niobium pentoxide used the resultant materials of the Step 3 (H) were named as in the following CFNb - cobalt ferrite with non-calcined niobium pentoxide and $CFNb_{Tcalc}$ cobalt ferrite with niobium pentoxide calcined at calcination temperature.

2.3 Characterization techniques

Surface and pore analyzer

The determination of the specific surface area was carried out for the characterization of porous and finely-dispersed solids [45]. Analysis of N_2 adsorption–desorption isotherms at 77 K were carried out with a Quantachrome NOVATouch XL4 adsorption analyser to determine the textural properties of prepared samples. The BET specific surface area (S_{BET}) was calculated by the Brunauer, Emmett, Teller method (BET). The external surface area (S_{ext}) and the micropore volume (V_{mic}) were obtained by using the *t*-method and employing the ASTM standard D-6556-01 to calculate the thickness (*t*). Then, the microporous surface area (S_{mic}) was calculated subtracting the S_{ext} from S_{BET} and the average pore width (W_{mic}) by approximation ($W=4\ V_{mic} / S_{mic}$). The total pore volume (V_{Total}) was determined at p/p^0=0.98.

Scanning Electron Microscopy (SEM) and Energy Dispersive Spectroscopy (EDS)

The topographic surface images were obtained using a scanning electron microscope model VEGA 3 LMU brand TESCAN, completed with a W 20 kV filament, 3.0 nm resolution, retractable SE and BSE detectors, low-vacuum mode (500 Pa) chamber with internal diameter of 230 mm and door opening of 148 mm, 5-axis compucentric stage, fully motorized, with X: 80mm, Y: 60mm and Z: 47mm movements, CCD camera for viewing the sample chamber and “chamberview” software, VegaTC operating software, data processing system and track-ball. The microscope is also equipped with a DES Detector, model AZTec Energy X-Act, resolution 130 eV, Oxford.

Point of zero charge (pHpzc)

The determination of pHpzc allows allows suppositions to be made about types of surface active centers and adsorption abilities of surfaces [46]. For this determination, approximately 0.09 g of material was added in 6 different Erlenmeyer with different initial pH values (pH0). The Erlenmeyer flasks were loaded with 15.0 mL of 0.01 mol L-1 Na2SO4 and their pH adjusted to different values (2.0, 4.0, 6.0, 8.0, 10.0 and 12.0) using 0.02 M NaOH and 0.02 mol L-1 H2SO4 solutions. The Erlenmeyer Flasks were then placed in an orbital shaker (TE-424, TECNAL) at 200 ± 3 rpm, 25 ± 2 °C. After stirring, the suspension was separated from the catalyst by means of a magnet and the final pH was measured (pHF). The pH of the point of zero charge was found at the intersection between the pH0 X pHF curve and the identity curve [34].

Photocatalysis

All photocatalytic tests were performed in the photocatalytic chamber. The reaction mixture was transferred to a glass reactor consisting of a cylindrical Pyrex cell surrounded by a water jacket (constant temperature of ~25 °C). The pH of the paracetamol solution (20.7 ± 2.2 mg L^{-1}) was adjusted with formic acid solutions and placed in the reactor, which was placed in the photocatalytic chamber. The solution has magnetic stirring using magnetic stirring plate and constant air flow. Finally, the catalyst was added to the solution and samples were taken at 0, 15, 30, 45, 60, 90, 120, 180 and 240 minutes.

3. Results and Discussion

BET surface area

The textural properties of the Nb_2O_5 samples, obtained by calcination at different temperatures, step 2 (E) of the synthesis, were determined and the results shown in Table 1.

Table 1 – Results of BET surface area of the calcined niobium pentoxide samples.

Samples	SBET (m^2/g)	Sext (m^2/g)	Smic (m^2/g)	Vmic (mm^3/g)	Vtotal (mm^3/g)
Nb	185	88	97	50.3	158
Nb100	178	103	75	39	163
Nb200	156	113	43	22.7	160
Nb300	134	106	28	14.5	145.1
Nb400	112	103	9	5.3	131.4
Nb500	69	69	0	0	118
Nb600	31	31	0	0	99.1

Evaluating the data given in Table 1 it is possible to conclude that S_{BET}, S_{mic} and V_{mic} decreases as the calcination temperature of Nb_2O_5 increases. The change in these values is related to the structure of Nb_2O_5, which, as already mentioned, is amorphous until heat treatment at 400 °C and, therefore, must have presented higher values up to this temperature. For temperatures above 500 °C the material may have been sintered, to form the pseudohexagonal and orthorhombic structures, or still if crowded decreasing the S_{BET} values, as shown in Table 1 .

In theory, it would be more interesting to use the material with higher S_{BET}, S_{mic} and V_{mic}, as it would better aggregate the cobalt ferrite (CF) particles and still have a higher surface area for active sites for catalysis. However, after mixing with the Fe^{3+} and Co^{2+} salts reagents and tangerine extract, there is another heat treatment step up to 600 °C, and this temperature may also influence the behavior of both the Nb_2O_5 and the final catalyst. In addition, it should be also taken into consideration the structure of Nb_2O_5, if was amorphous, pseudohexagonal, hexagonal or orthorhombic, which for application in photocatalysis may have great influence.

According to the literature, the materials containing niobium pentoxide and cobalt ferrite have specific surface area BET (S_{BET}) according to the values mentioned in Table 2. However, there is not specific comparison for the material $CoFe_2O_4@Nb_2O_5$, as it is an innovation.

In general, it is possible to conclude that as calcination temperature of Nb_2O_5 increases the value for S_{BET} decreases. And when niobium supports some metal, these values will depend on both the metal content and the calcination temperature. The $CoFe_2O_4$ have low S_{BET} values, however if supported on a highly porous material (such as graphite) it can increase the S_{BET} value, as observed in Table 2.

Table 2 - SBET values reported in the literature for Nb2O5 and CoFe2O4 compounds

Material	SBET (m^2/g)	T calcination	Reference
Nb_2O_5	24	500 °C	[22]
Nb_2O_5	81 ± 8	100 °C	47
	36 ± 4	500 °C	
	22 ± 2	600 °C	
	13 ± 1	800 °C	
Amorphous-Nb_2O_5	129.6	450 °C	48
Pseudohexagonal-Nb_2O_5	57.8	600 °C	
Orthorhombic-Nb_2O_5	43.0	800 °C	
Nb_2O_5/C nanocomposites	98.33	600 °C	49
Fe/Nb_2O_5			50
0.5% Fe	20.26	400 °C	
1.5% Fe	64.90	400 °C	
0.3% Fe	43.44	500 °C	
1.0% Fe	149.63	500 °C	
1.7% Fe	43.44	500 °C	
0.5% Fe	148.83	600°C	
1.5% Fe	21.24	600°C	
Cobalt ferrite core and a graphitic shell	330	500 °C	51
$CoFe_2O_4$	44	400 °C	52

Figure 2 shows the comparison of all the adsorption isotherms for the samples of niobium pentoxide calcined up to 600 °C. To characterize the catalysts in terms of the type of material, the IUPAC (International Union of Pure and Applied Chemistry) provides a classification for physisorption isotherms and associated hysteresis loops [53].

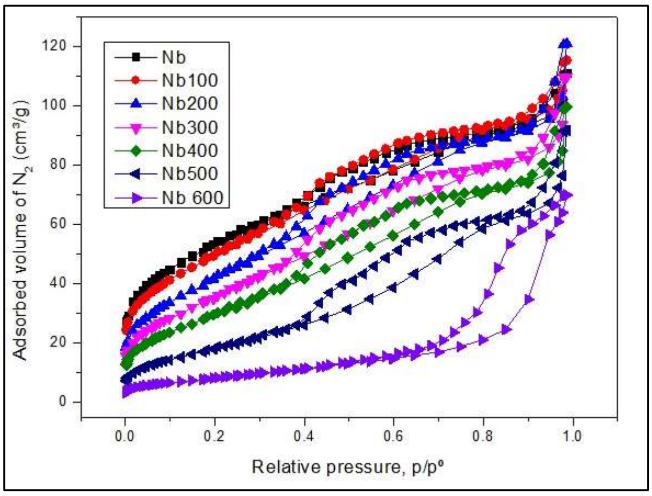

Figure 2 - Adsorption isotherms for calcined niobium pentoxide samples.

According to the IUPAC classification for physisorption isotherms and associated hysteresis loops and the hysteresis loop, the Nb_2O_5 calcined up to 500 °C (graphs Nb, Nb100, Nb200, Nb300, Nb400 and Nb500) are IVa - H4 and the Nb_2O_5 calcined at 600 °C (Nb600) are IVa-H5.

Point of zero charge (pHpzc)

Depending on the pH, the catalyst surface may be uncharged, negatively or positively charged. The isoelectric point, also known as PZC (point of zero charge), is the pH at which the suspended particles have zero net charge and no mobility in the electric field (pH_{PZC}) [54]. Following the procedure described in the methodology, the pH_{PZC} was obtained by intercepting the experimental curves of each sample with the identity curve.

Among the evaluated catalyst samples, two curve profiles for pH_{PZC} were presented around pH 4.0, which were separated in graphs A and B of Figure 3. However, both profiles showed neutral and similar pH_{PZC} between 6 and 7.5.

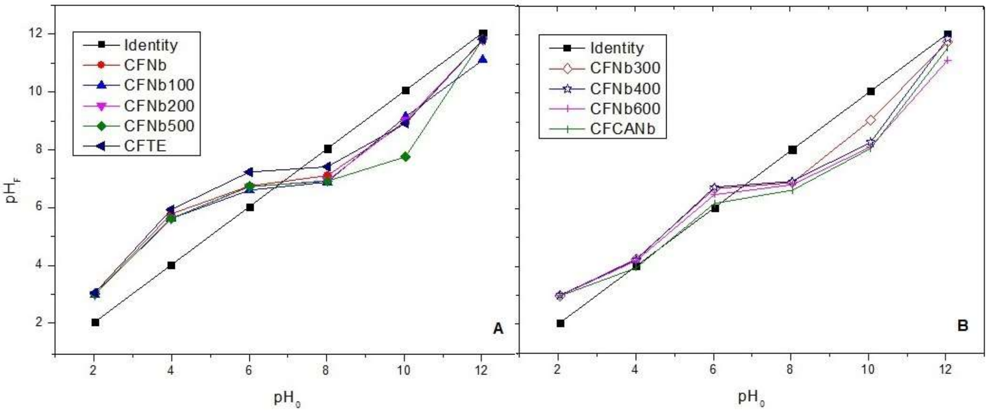

Figure 3 - pHPZC curves of the tested materials.

From the results of pH_{PZC} it is possible to notice that when the cobalt ferrite was produced without the addition of niobium (CFTE) it presented a pH_{PZC} value slightly higher than the other values. In addition, comparing CFCANb with CFNb, the first one that was synthesized with commercial citric acid showed a slightly lower pH_{PZC} value, in relation even with the other samples synthesized with the extract of the tangerine peels, suggesting that the extract gave to the synthesized material some particularity in its structure.

Scanning Electron Microscopy (SEM)

The working principle of the SEM is related to an interaction between electrons and matter. The Scanning Electron microscope contains a source that generates an electron beam that is continuously fired in the sample during the test, scanning its surface. Thus, through a detector present in the equipment, it is possible to analyze the electron energies during an interaction between them and the surface, which are interpreted by the equipment and generate images like as in Figure 4, representing the characterization of the samples CFNb, $CFNb_{100}$, $CFNb_{200}$, $CFNb_{300}$, $CFNb_{400}$, $CFNb_{500}$, $CFNb_{600}$ and

CFCANb. It is possible to observe clusters of nanomaterials, very typical of materials that have magnetic properties [16,18,55-58]. In addition, it is possible to observe the surface difference of the CFCANb sample, which was produced with commercial citric acid instead with the tangerine extract. It apparently has a planar surface, possibly because it formed larger clusters (in blocks). In contrast, the other samples could still be divided into two groups due to apparent small superficial similarity, on the one hand CFNb, CFNb$_{100}$, CFNb$_{200}$ and CFNb$_{300}$ and on the other CFNb$_{400}$, CFNb$_{500}$ and CFNb$_{600}$. This may be related to the calcination temperature of Nb_2O_5 before synthesis.

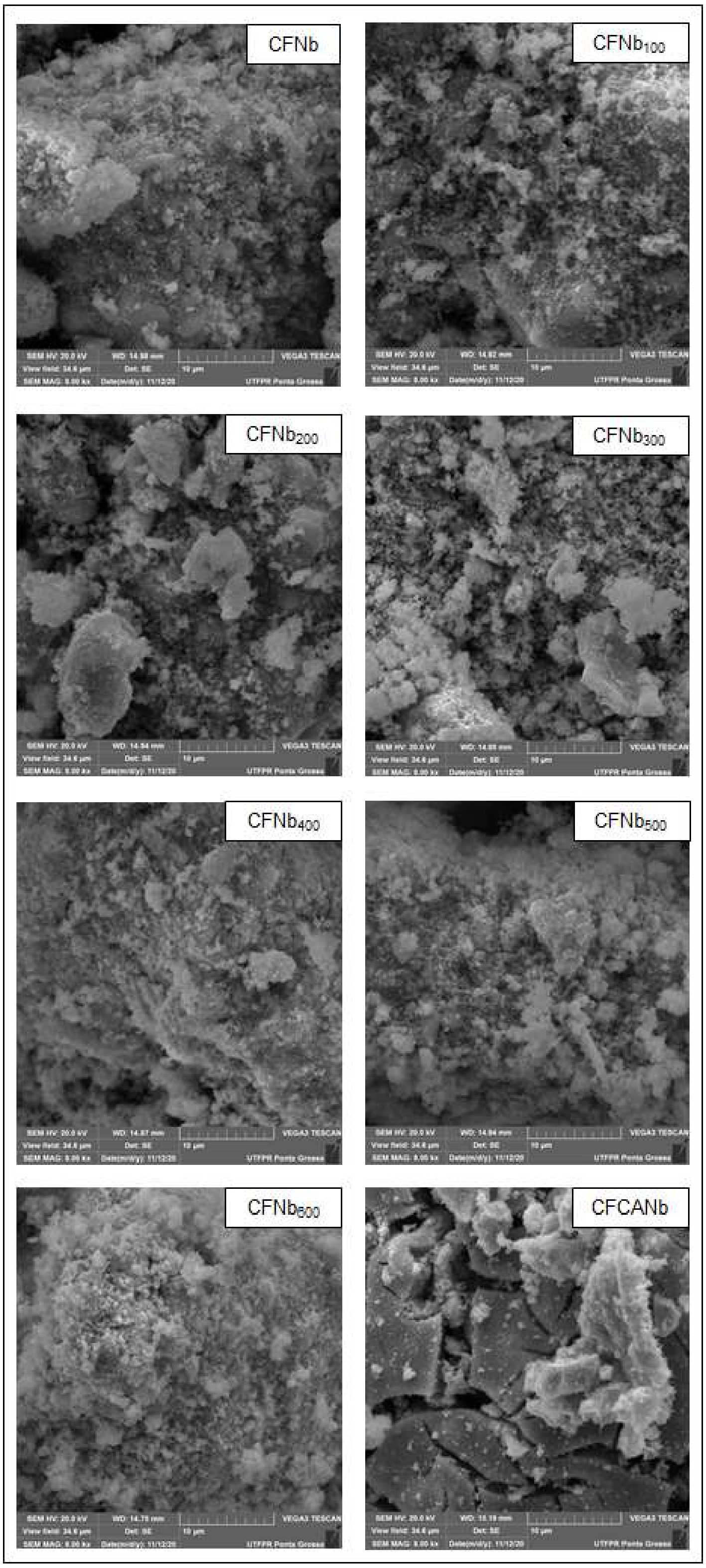

Figure 4 – SEM images of the samples.

Energy Dispersive Spectroscopy (EDS), which allows the detection and fraction of chemical elements on the surface, was performed for catalysts CFNb, $CFNb_{100}$, $CFNb_{200}$, $CFNb_{300}$, $CFNb_{400}$, $CFNb_{500}$ and $CFNb_{600}$. The fraction of each component is summarized in the Table 3, as well as the mean and standard deviation per component.

Table 3 - Components percentage in weight, resulting from EDS analysis.

	CFNb	**CFNb100**	**CFNb200**	**CFNb300**	**CFNb400**	**CFNb500**	**CFNb600**	**Mean ± sd**
O (W %)	33.6	35.7	32.7	30.2	31.1	31.6	27.8	31.8 ± 2.5
Fe (W %)	27.3	26.6	24.4	31.6	27.8	34.7	42.9	30.8 ± 6.4
Nb (W %)	24.8	27.2	32.0	15.9	25.8	17.7	14.3	22.5 ± 6.6
Co (W %)	14.0	10.3	10.9	22.2	15.3	15.8	14.7	14.7 ± 3.9

It should be bear in mind that it was expected to obtain the synthesis of nanomaterials of functionalized cobalt ferrite in niobium pentoxide of supposed molecular formula $CoFe_2O_4@Nb_2O_5$ and that the atomic weight of one mole of this component would be about 500.44 u (assuming Co = 58.93 u, Fe = 55.845 u, O = 16 u and Nb = 92.91 u). Recalling that the synthesis was performed with 50% w/w of $CoFe_2O_4$ and Nb_2O_5, the theoretical fraction by weight of each element would be O = 28.68± 0.00%, Fe = 23.92 ± 0.02%, Nb = 34.78 ± 0.04% and Co = 12.62 ± 0.01%. These values are considered close to the values obtained considering the standard deviation for more and for less, therefore, it can be considered that $CoFe_2O_4@Nb_2O_5$ was really the synthesized material.

X-ray diffraction (XRD) analysis

The interpretation of the XRD analysis of the synthesized samples were done using the standards published by the Joint Committee on Powder Diffraction Standards – International Center for Diffraction Data (JCPDS - ICDD) cards No. 22-1086, No.28-0317 and No.30-0873 that concern cobalt ferrite, pseudo-hexagonal phase (TT-Nb_2O_5) and orthorhombic phase (T-Nb_2O_5) of niobium pentoxide, respectively.

According to the aforementioned standards (Figure 5), which belong to face-centered cubic spinel type (Fd - 3m), the cobalt ferrite has an estimated lattice parameter a = b = c = 8.38 Å. In addition, this compound is characterized by having peaks between 2Θ° = 15° and 70° as follows: 18.289°, 30.085°, 35.438°, 37.057°, 43.059°, 53.446°, 56.975°, 62.587°, which correspond to the indices of Miller (111), (220), (311), (222), (400), (422), (511) and (440), respectively [15,59,60].

On the other hand, the pseudo-hexagonal and orthorhombic phases of niobium pentoxide have very similar patterns, Figure 6. The TT-Nb_2O_5 (JCPDS – ICDD 28-0317), with lattice parameters a = 3.607 Å, b = 3.607 Å, c = 3.925 Å; space group: P6/mmm, has the Miller indices (001), (100), (101), (002), (110), (102) and (112) [61-63]. The T-Nb2O5 (JCPDS – ICDD 30-0873), with lattice parameters a = 6,175 Å, b = 29,175 Å, c = 3,930 Å and space group: Pbam, has typical diffraction peaks located at 22.7°, 28.5°, 36.7°, 46.2°, 50.6°, 55.1° and 71.0°, which correspond to the Miller indices (001), (180) , (181), (002), (380), (182) and (382), respectively[49,64,65].

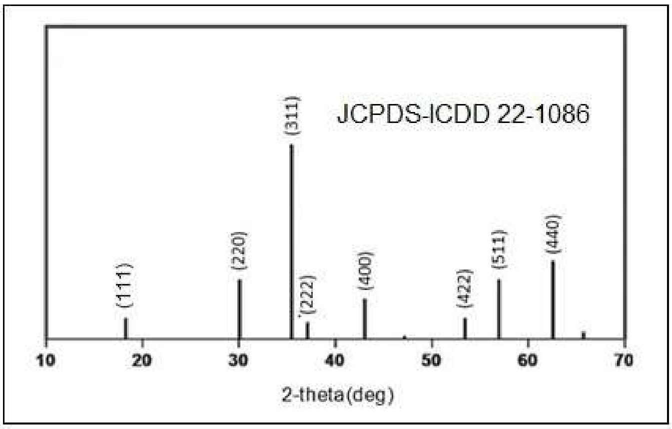

Figure 5 - Standard X-ray diffractogram of cobalt ferrite. [15, 59,60, adapted].

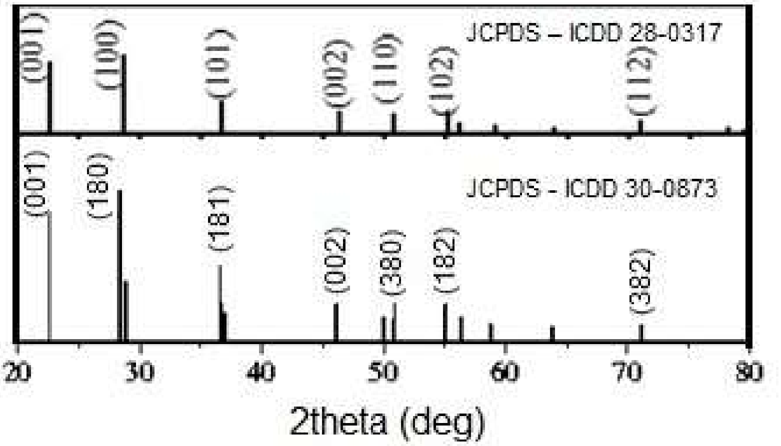

Figure 6 - Standard X-ray diffractogram of the TT-Nb2O5 (JCPDS – ICDD No. 28-0317) and T-Nb2O5 (JCPDS – ICDD No. 30-0873) [49,63,64, adapted].

Figure 7 shows the X-ray diffractograms obtained for the samples CFNb, $CFNb_{100}$, $CFNb_{200}$, $CFNb_{300}$, $CFNb_{400}$, $CFNb_{500}$, $CFNb_{600}$ and CFCANb. In this figure, the peaks related to ferrite were identified as cobalt and niobium pentoxide, represented by the acronyms CF and Nb, respectively. Comparing the patterns with the obtained results, it is observed that all samples have peaks in the diffraction angles for the mentioned components. Identifying the cobalt ferrite, the peaks appear around 2theta angles of 18.3°, 30.3°, 35.5°, 37.1°, 43.1°, 53.5° and 62.6°, corresponding to the mentioned pattern. For the identification of niobium pentoxide, it was observed peaks for the 2theta angles of 22.6°, 28.4°, 36.4°, 46.2°, 50.2°, 55.2° and 71.1°, which correspond to the aforementioned patterns. By this way it is possible to identify that the obtained samples refer to the material of cobalt ferrite functionalized in niobium pentoxide.

Furthermore, it is possible to observe some details, such as the increase in intensity around the angles 2theta of 46.2°, 55.2° and 71.1°, which increase as the Nb_2O_5 calcination temperature increases in step 2 of the synthesis, being more intense for temperatures between 400 and 600 °C. This difference is possibly related to the structure of niobium pentoxide in the material.

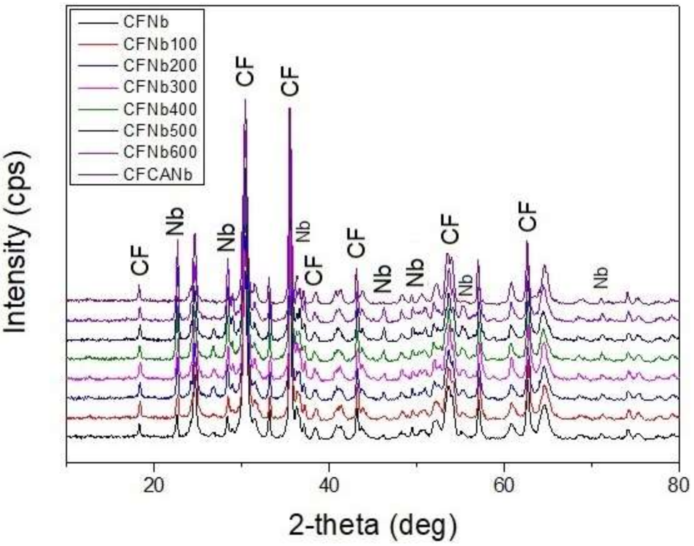

Figure 7 - Components identification in the diffractogram (cobalt ferrite = CF; niobium pentoxide = Nb)

One way to better define the structure obtained is by using a characterization refinement to compare lattice parameters, which for each structure has its specificity. Another way is to manually calculate the lattice parameter (a) using the classical formula given by equation (1) [66].

$$\frac{1}{d^2} = \frac{h^2 + k^2 + l^2}{a^2} \quad (1)$$

where h, k and l are parameters related to the Miller index of the structure (i.e. (180), so h is 1, k is 8 and l is 0); d is the distance between one plane and the other, which can be calculated by the Bragg's law, equation (2).

$$2d \sin \theta = n\lambda \quad (2)$$

where λ is the wavelength of the X-ray radiation (all diffraction patterns shown in this work were performed with CuKa radiation, so λ is 0.154 nm or 1.54 Å); θ is the diffraction angle in radians; and n is constructive interference (n=1,2,3,...,n). Substituting equation (1) on equation (2), equation (3) is obtained.

$$a = \lambda \frac{[h^2 + k^2 + l^2]^{1/2}}{2 \sin \theta} \quad (3)$$

The values of the calculated lattice parameters were tabulated for better comparison with the values established by the cited standards,

Table 4. It can be observed that the values of the lattice parameters for cobalt ferrite were very close to the values established as standard. As for niobium pentoxide, the values were closer to TT-Nb_2O_5 than to T-Nb_2O_5, which concerns the pseudo-hexagonal phase, which is possibly the predominant phase in the material obtained.

Table 4 – Results of the lattice parameters.

Sample	$CoFe_2O_4$ (a=8.38 Å)	TT-Nb_2O_5 (a=3.61 Å)	T-Nb_2O_5 (b=29,17 Å)
CFNb	8.38	3.53	25.38
CFNb100	8.36	3.51	25.31
CFNb200	8.37	3.52	25.40
CFNb300	8.37	3.51	25.31
CFNb400	8.37	3.53	25.35
CFNb500	8.37	3.51	25.32
CFNb600	8.36	3.51	25.35
CFCANb	8.37	3.03	20.10

Further exploring the results of the XRD characterization, the average crystallite sizes (L) were calculated using the Scherrer's equation, the results are shown in Table 5. It is possible to observe that the thermal treatment of niobium (step 2) did not significantly influence the average crystallite sizes of the material. As a general rule, the higher the temperature, the larger the crystallite size. The material with the largest average crystallite size (33.85 nm) was synthesized with commercial citric acid, instead of tangerine extract (CFCANb).

Table 5 - The average sizes of crystallites (D), calculated using the Scherrer's equation.

Samples	L (nm)
CFNb	24.10
CFNb100	22.78
CFNb200	25.39
CFNb300	24.82
CFNb400	26.34
CFNb500	27.36
CFNb600	28.13
CFCANb	33.85

Evaluating the characterizations as a whole, it is possible to conclude that the thermal treatment (step 2) was not so impacting in the formation of the catalysts and only small differences are noticed, all samples being cobalt ferrite functionalized in niobium pentoxide as predicted ($CoFe_2O_4$@Nb_2O_5).

Photocatalytic tests

The preliminary tests using a mercury vapor lamp of 125W of power and radiation measured around 11 mW cm-², were realized, for all catalysts synthetized. However, the results obtained to photocatalytic activity were low (<5%). As the physical characterizations of the catalysts showed that the structures were very similar, independent of the previous calcination of niobium pentoxide. So, it was decided to optimize some operating parameters to the simplest catalyst in the analysis of paracetamol degradation. In the synthesis of the CFNb is not necessary previously calcination of niobium pentoxide, for this reason the synthesis this compound is cheaper, due to the fact that it uses less energy and time to synthesize it.

pH Influence

To verify the pH influence, tests were performed for different pH ranges (acid-base). The results obtained were for pH 2,4,6 of degradation of paracetamol 34%, 30%, and 23%, respectively (Figure 8). It was observed that pH was a factor that significantly influenced the Paracetamol degradation.

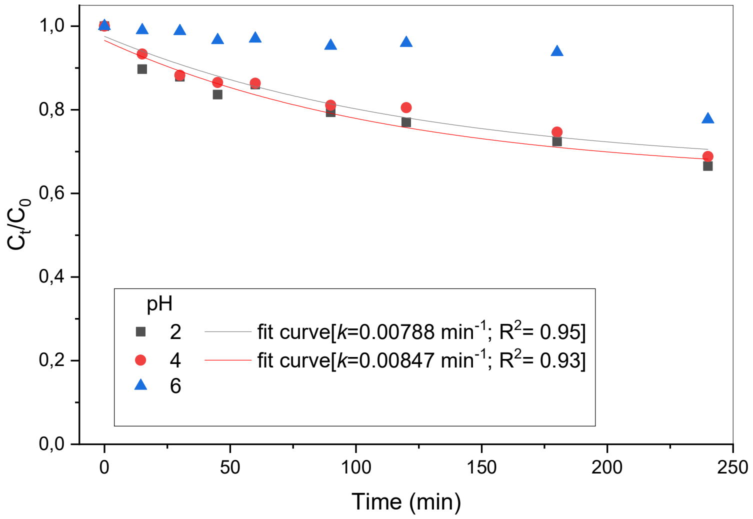

Figura 8. Paracetamol degradation in different pH [300 mg L^{-1}; 20.7 ppm, CFNb].

On the other hand, some authors indicated in the literature the optimal pH for different catalysts. Yang et al. (2008) reported that the paracetamol degradation rate slowly increased between pH 3.5 and 9.5, but significantly decreased with increasing pH between 9.5 and 11.0, using TiO2 as a catalyst. González-Labrada et al. (2016) studied the paracetamol degradation by different processes based on ultraviolet radiation (photolysis, photo-oxidation with hydrogen peroxide, photo-Fenton reaction, and heterogeneous photocatalysis) with TiO2 [67]. The results indicated that the during the oxidation, the pH of the reaction medium usually decreased due to the formation of acidic intermediates (final pH ranging between 3.0 and 5.0). Irrespective of the pH value, the degradation rate of paracetamol by photolysis at O > 280 nm was almost negligible, a maximum conversion of 4.2% being achieved after 5 hours with pH0 = 2.6. It is known that the hydrolysis of paracetamol is proton and hydroxyl ion catalyzed, while this breakdown process is minimal at a pH close to 6..

Effect of catalyst concentration

Figure 9 shows the results obtained from experimental tests using different catalyst concentrations. The results indicated that at pH 5 the amount of catalyst has no effect on the paracetamol degradation(~11%). However, when the pH studied is pH 2 with a lower amount of catalyst, a better paracetamol degradation performance was obtained (100% - 158 mg L^{-1}; and 74% 441 mg L^{-1}). Possibly this was due to the blocking of radiation than the greater amount of catalyst.

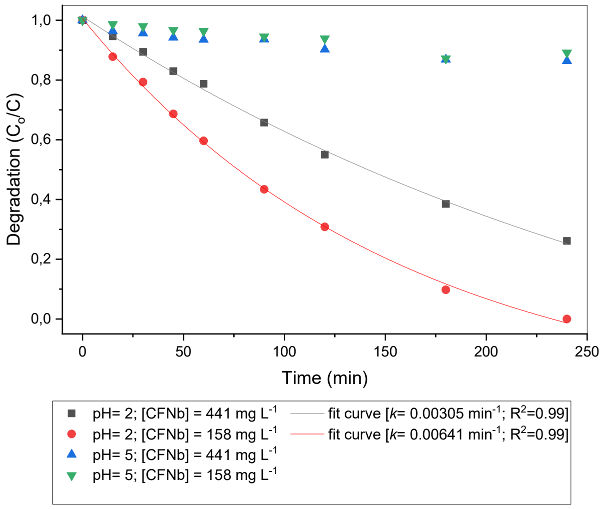

Figure 9. Catalyst concentration influence on photocatalytic paracetamol removal.

Adsorption and photolysis

The adsorption and photolysis tests results are presented in Figure 10. As it can be seen in Figure x , the pollutant concentration remained virtually constant throughout the 240 minutes of adsorption and photolysis. Indicating the need to use the catalyst in the degradation process.

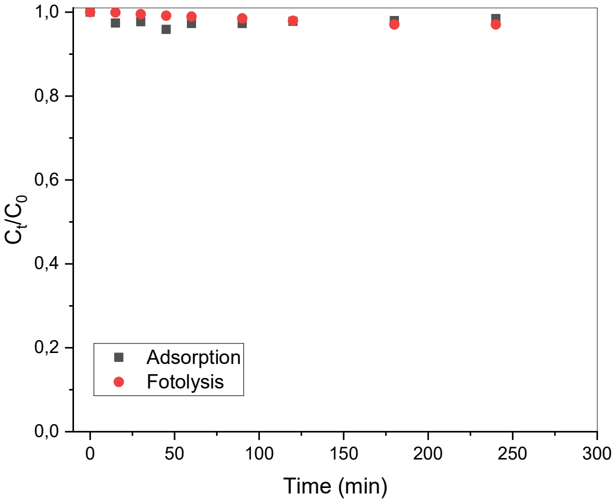

Figure. 10. Adsorption and photolysis results.

4. Conclusions

From the results obtained it is concluded that was successfully achieved the objective of creating a methodology via green synthesis, using extract from tangerine peel to obtain nanocatalysts composed of cobalt ferrite and niobium pentoxide. The methodology created, as well as the combination of elements considered, was worthy to patent attempt for the method and product obtained. Among several advantages of the synthesis, it can be highlighted the reuse of biomass residues, the low cost to obtain the material and the value added to a component richly disposed in the Brazilian territory (niobium).

The catalytic materials were active in the studied photocatalytic reaction of paracetamol degradation. Several experiments allowed to find the optimum operating conditions using formic acid to adjust pH 2, catalyst concentration of 158 mg.L^{-1} and mercury vapor lamp power of 250 W. Under these conditions, for the catalyst CFNb, degradation of 100% was obtained, fulfilling the objective of finding a photocatalysis conditions that would degrade the emerging pollutant paracetamol.

5. References

1. Rutger A. van Santen. *Theoretical Heterogeneous Catalysis*. 5, (World Scientific, 1991).
2. Ameta, R. & Ameta, S. C. *Nanoparticles and Catalysis*. (Wiley, 2007).

3. Ribeiro, R. S. *et al.* Hybrid magnetic graphitic nanocomposites towards catalytic wet peroxide oxidation of the liquid effluent from a mechanical biological treatment plant for municipal solid waste. *Appl. Catal. B Environ.* 219, 645–657 (2017).
4. United States Environmental Protection Agency. Basics of Green Chemistry. Available at: https://www.epa.gov/greenchemistry/basics-green-chemistry#:~:text=Definition of green chemistry,-Green chemistry is&text=Green chemistry%3A&text=Reduces the negative impacts of,to reduce their intrinsic hazards.
5. Anastas, P. & Warner, J. 12 Principles of Green Chemistry. *ACS Chemistry for life* (1998). Available at: https://www.acs.org/content/acs/en/greenchemistry/principles/12-principles-of-green-chemistry.html.
6. Kharissova, O. V., Kharisov, B. I., Oliva González, C. M., Méndez, Y. P. & López, I. Greener synthesis of chemical compounds and materials. *R. Soc. Open Sci.* 6, 191378 (2019).
7. Gingasu, D. *et al.* Green synthesis methods of CoFe2O4 and Ag-CoFe2O4 nanoparticles using Hibiscus extracts and their antimicrobial potential. *J. Nanomater.* (2016). doi:http://dx.doi.org/10.1155/2016/2106756
8. Gingasu, D. *et al.* Synthesis of nanocrystalline cobalt ferrite through soft chemistry methods: A green chemistry approach using sesame seed extract. *Mater. Chem. Phys.* 182, 219–230 (2016).
9. Li, G.-L. *et al.* Tangerine peel-derived carbon supported manganese oxides catalyst for oxygen reduction reaction. *Appl. Surf. Sci.* 450, 251–259 (2018).
10. Durmuş, A., Çolak, H. & Karaköse, E. Production and examination of ZnO thin film for first time using green synthesized method from aqueous Citrus reticulata peel extract. *J. Alloys Compd.* 809, 151813 (2019).
11. Rueda, D. *et al.* Low-cost tangerine peel waste mediated production of Titanium Dioxide Nanocrystals: Synthesis and characterization. *Environ. Nanotechnology, Monit. Manag.* 13, 100285 (2020).
12. Ituen, E., Ekemini, E., Yuanhua, L. & Singh, A. Green synthesis of Citrus reticulata peels extract silver nanoparticles and characterization of structural, biocide and anticorrosion properties. *J. Mol. Struct.* 1207, 127819 (2020).
13. Rani, B. J. *et al.* Ferrimagnetism in cobalt ferrite (CoFe2O4) nanoparticles. *Nano-Structures and Nano-Objects* 14, 84–91 (2018).
14. Carvalho, F. E., Lemos, L. V., Migliano, A. C. C., Machado, J. P. B. & Pullar, R. C. Structural and complex electromagnetic properties of cobalt ferrite (CoFe2O4) with an addition of niobium pentoxide. *Ceram. Int.* 44, 915–921 (2018).
15. Long, N. V. *et al.* Synthesis and magnetism of hierarchical iron oxide particles. *Mater. Des.* 86, 797–808 (2015).
16. Sonu *et al.* Review on augmentation in photocatalytic activity of CoFe2O4 via heterojunction formation for photocatalysis of organic pollutants in water. *J. Saudi Chem. Soc.* 23, 1119–1136 (2019).
17. Amiri, M., Salavati-Niasari, M., Akbari, A. & Gholami, T. Removal of malachite green (a toxic dye) from water by cobalt ferrite silica magnetic nanocomposite: Herbal and green sol-gel autocombustion synthesis. *Int. J. Hydrogen Energy* 42, 24846–24860 (2017).
18. Shi, Z. *et al.* Mesoporous superparamagnetic cobalt ferrite nanoclusters: Synthesis, characterization and application in drug delivery. *J. Magn. Magn. Mater.* 498, 166222 (2020).
19. Amiri, M., Salavati-Niasari, M., Pardakhty, A., Ahmadi, M. & Akbari, A. Caffeine: A novel green precursor for synthesis of magnetic CoFe2O4 nanoparticles and pH-sensitive magnetic alginate beads for drug delivery. *Mater. Sci. Eng. C* 76, 1085–1093 (2017).
20. Kefeni, K. K., Mamba, B. B. & Msagati, T. A. M. Magnetite and cobalt ferrite nanoparticles used as seeds for acid mine drainage treatment. *J. Hazard. Mater.* 333, 308–318 (2017).
21. Pessoa, C. No final das contas, o que é nióbio? *TecMundo* (2018). Available at: https://www.tecmundo.com.br/ciencia/132827-final-contas-niobio.htm. (Accessed: 21st April 2020)
22. Silva, M. K., Marques, R. G., Machado, N. R. C. F. & Santos, O. A. A. Evaluation of Nb2O5 and Ag/Nb2O5 in the photocatalytic degradation of dyes from textile industries. *Brazilian J. Chem. Eng.* 19, 359–363 (2002).
23. Castro, D. C. *et al.* Synthesis and Characterization of Mesoporous Nb_2O_5 and Its Application for Photocatalytic Degradation of the Herbicide Methylviologen. *J. Braz. Chem. Soc.* 27, 303–313 (2016).
24. Xiang, W., Han, X., Astorsdotter, J. & Farrauto, R. Catalysts Promoted with Niobium Oxide for Air Pollution Abatement. *Catalysts* 7, 144 (2017).
25. Petre, A. ., Perdigón-Melón, J. ., Gervasini, A. & Auroux, A. Characterization and reactivity of group III oxides supported on niobium oxide. *Catal. Today* 78, 377–386 (2003).
26. Guarino, M. E., Albuquerque, R. V. T. De, Pereira, C. A. S. & Urquieta-gonzález, E. A. Avaliação da eficiência de catalisadores à base de cobre, ferro, níquel e cobalto , suportados em óxido de nióbio, na redução do óxido nítrico por monóxido de carbono. *Exatas Online* 5, 13–28 (2014).
27. Xu, D. *et al.* Cobalt-free niobium-doped barium ferrite as potential materials of dense ceramic membranes for oxygen separation. *J. Memb. Sci.* 455, 75–82 (2014).
28. Amjad, U., Gonçalves Lenzi, G., Camargo Fernandes-Machado, N. R. & Specchia, S. MgO and Nb2O5 oxides used as supports for Ru-based catalysts for the methane steam reforming reaction. *Catal. Today* 257, 122–130 (2015).
29. ALI, S., MOHD ZABIDI, N. A. & SUBBARAO, D. Effect of niobium promoters on iron-based catalysts for

Fischer-Tropsch reaction. *J. Fuel Chem. Technol.* 40, 48–53 (2012).

30. Ghosh, M., Swain, K. K. & Verma, R. Interaction of niobium with iron-oxide colloids and the role of humic acid. *J. Environ. Radioact.* 178–179, 101–109 (2017).
31. Ramchandra Kiran, R., Mondal, R. A., Dwevedi, S. & Markandeyulu, G. Structural, magnetic and magnetoelectric properties of Nb substituted Cobalt Ferrite. *J. Alloys Compd.* 610, 517–521 (2014).
32. Carvalho, F. E., Lemos, L. V., Migliano, A. C. C., Machado, J. P. B. & Pullar, R. C. Structural and complex electromagnetic properties of cobalt ferrite (CoFe2O4) with an addition of niobium pentoxide. *Ceram. Int.* 44, 915–921 (2018).
33. *Handbook of Heterogeneous Catalysis*. 1, (Wiley-VCH Verlag GmbH & Co. KGaA, 2008).
34. Silva, A. S. Treatment of wastewater containing pharmaceutical compounds by catalytic wet peroxide oxidation using clay-based materials as catalysts. (Thesis report (Master Degree in Chemical Engineering).Instituto Politécnico de Bragança, 2019).
35. Gomes, H. T. *et al.* The role of activated carbons functionalized with thiol and sulfonic acid groups in catalytic wet peroxide oxidation. *Appl. Catal. B Environ.* 106, 390–397 (2011).
36. Zhu, D. & Zhou, Q. Action and mechanism of semiconductor photocatalysis on degradation of organic pollutants in water treatment: A review. *Environ. Nanotechnology, Monit. Manag.* 12, 100255 (2019).
37. Zhang, J., Tian, B., Wang, L., Xing, M. & Lei, J. *Photocatalysis: Fundamentals, Materials and Applications*. 100, (Springer Singapore, 2018).
38. Fontana, K. B., Lenzi, G. G., Seára, E. C. R. & Chaves, E. S. Comparision of photocatalysis and photolysis processes for arsenic oxidation in water. *Ecotoxicol. Environ. Saf.* 151, 127–131 (2018).
39. Yu, M. *et al.* Intimate coupling of photocatalysis and biodegradation for wastewater treatment: Mechanisms, recent advances and environmental applications. *Water Res.* 175, 115673 (2020).
40. Napoleão, D. C. *et al.* Degradação do contaminante emergente paracetamol empregando processos oxidativos avançados. *Rev. Eletrônica em Gestão Educ. e Tecnol. Ambient.* 19, 725–734 (2015).
41. Paumo, H. K. *et al.* TiO2 assisted photocatalysts for degradation of emerging organic pollutants in water and wastewater. *J. Mol. Liq.* 115458 (2021). doi:10.1016/j.molliq.2021.115458
42. FARMACOCINÉTICA PARACETAMOL. (2016). Available at: https://www.bulas.med.br/p/detalhamento-das-bulas/1187419/farmacocinetica+paracetamol.htm.
43. Nava, O. J. *et al.* Fruit peel extract mediated green synthesis of Zinc Oxide nanoparticles. *J. Mol. Struct.* (2017). doi:10.1016/j.molstruc.2017.06.078
44. Oliveira, J. R. P. *et al.* Carbon-based magnetic nanocarrier for controlled drug release: a green synthesis approach. *J. Carbon Res.* 5, (2018).
45. 3P-instrument. BET surface area. (2020). Available at: https://www.3p-instruments.com/measurement-methods/bet-surface-area/#measurement-methods-bet-surface-area. (Accessed: 16th December 2020)
46. Poghossian, A. A. Determination of the pHpzc of insulators surface from capacitance–voltage characteristics of MIS and EIS structures. *Sensors Actuators B Chem.* 44, 551–553 (1997).
47. Falk, G. *et al.* Microwave-assisted synthesis of Nb2O5 for photocatalytic application of nanopowders and thin films. *J. Mater. Res.* 32, 3271–3278 (2017).
48. Li, S., Xu, Q., Uchaker, E., Cao, X. & Cao, G. Comparison of amorphous, pseudohexagonal and orthorhombic Nb 2 O 5 for high-rate lithium ion insertion. *CrystEngComm* 18, 2532–2540 (2016).
49. Zeng, G.-Y. *et al.* Fabrication of Nb 2 O 5 /C nanocomposites as a high performance anode for lithium ion battery. *Chinese Chem. Lett.* 28, 755–758 (2017).
50. Fidelis, M. *et al.* Experimental Design and Optimization of Triclosan and 2.8-Diclorodibenzeno-p-dioxina Degradation by the Fe/Nb2O5/UV System. *Catalysts* 9, 343 (2019).
51. Ribeiro, R. S. *et al.* Enhanced performance of cobalt ferrite encapsulated in graphitic shell by means of AC magnetically activated catalytic wet peroxide oxidation of 4-nitrophenol. *Chem. Eng. J.* 376, 120012 (2019).
52. Ianoș, R. Highly sinterable cobalt ferrite particles prepared by a modified solution combustion synthesis. *Mater. Lett.* 135, 24–26 (2014).
53. Thommes, M. *et al.* Physisorption of gases, with special reference to the evaluation of surface area and pore size distribution (IUPAC Technical Report). *Pure Appl. Chem.* 87, 1051–1069 (2015).
54. Faraji, M., Yamini, Y. & Rezaee, M. Magnetic nanoparticles: synthesis, stabilization, functionalization, characterization, and applications. *J. Iran. Chem. Soc.* 7, 1–37 (2010).
55. Machado, S., Pacheco, J. G., Nouws, H. P. A., Albergaria, J. T. & Delerue-Matos, C. Characterization of green zero-valent iron nanoparticles produced with tree leaf extracts. *Sci. Total Environ.* 533, 76–81 (2015).
56. Huang, L., Weng, X., Chen, Z., Megharaj, M. & Naidu, R. Green synthesis of iron nanoparticles by various tea extracts: Comparative study of the reactivity. *Spectrochim. Acta Part A Mol. Biomol. Spectrosc.* 130, 295–301 (2014).
57. Harshiny, M., Iswarya, C. N. & Matheswaran, M. Biogenic synthesis of iron nanoparticles using Amaranthus dubius leaf extract as a reducing agent. *Powder Technol.* 286, 744–749 (2015).
58. Makarov, V. V. *et al.* Biosynthesis of Stable Iron Oxide Nanoparticles in Aqueous Extracts of Hordeum vulgare

and Rumex acetosa Plants. *Langmuir* 30, 5982–5988 (2014).

59. Sajjia, M., Oubaha, M., Prescott, T. & Olabi, A. G. Development of cobalt ferrite powder preparation employing the sol–gel technique and its structural characterization. *J. Alloys Compd.* 506, 400–406 (2010).
60. Purnama, B., Wijayanta, A. T. & Suharyana. Effect of calcination temperature on structural and magnetic properties in cobalt ferrite nano particles. *J. King Saud Univ. - Sci.* 31, 956–960 (2019).
61. He, J. *et al.* Hydrothermal growth and optical properties of Nb 2 O 5 nanorod arrays. *J. Mater. Chem. C* 2, 8185–8190 (2014).
62. Liu, M. & Xue, D. Large-scale fabrication of H2(H2O)Nb2O6 and Nb2O5 hollow microspheres. *Mater. Res. Bull.* 45, 333–338 (2010).
63. Morawa Eblagon, K., Malaika, A., Ptaszynska, K., Pereira, M. F. R. & Figueiredo, J. L. Impact of Thermal Treatment of Nb2O5 on Its Performance in Glucose Dehydration to 5-Hydroxymethylfurfural in Water. *Nanomaterials* 10, 1685 (2020).
64. Liao, J. *et al.* Controlling the morphology, size and phase of Nb2O5 crystals for high electrochemical performance. *Chinese Chem. Lett.* 29, 1785–1790 (2018).
65. Seo, H., Kim, K. & Kim, J.-H. Spherical Sb Core/Nb2O5-C Double-Shell Structured Composite as an Anode Material for Li Secondary Batteries. *Energies* 13, 1999 (2020).
66. Yakubu, A., Abbas, Z., Ibrahim, N. & Hashim, M. Effect of Temperature on Structural, Magnetic and Dielectric Properties of Cobalt Ferrite Nanoparticles Prepared via Co-precipitation Method. *Phys. Sci. Int. J.* 8, 1–8 (2015).

67 González-Labrada K., Quesada-Peñate I., Velichkova A. F., JulcourLebigue C., Andriantsiferana C., et al.. Degradation of paracetamol in aqueous solution: comparison of different uv induced advanced oxidation. Lat. Am. Appl. Res., 3, 115-120 (2016).